INTERNATIONAL JOURNAL OF NUMERICAL METHODS IN FLUIDS, VOL.20, 1363–1380 (1995)

A HYBRID FINITE-ELEMENT–VOLUME-OF-FLUID METHOD FOR SIMULATING FREE SURFACE FLOWS AND INTERFACES

F. MASHAYEK AND N. ASHGRIZ

Department of Mechanical and Aerospace Engineering, State University of New York at Buffalo, Buffalo, NY 14260, U.S.A.

SUMMARY

A numerical technique is developed for the simulation of free surface flows and interfaces. This technique combines the strength of the finite element method (FEM) in calculating the field variables for a deforming boundary and the versatility of the volume-of-fluid (VOF) technique in advection of the fluid interfaces. The advantage of the VOF technique is that it allows the simulation of interfaces with large deformations, including surface merging and breaking. However, its disadvantage is that in solving the flow equations, it cannot resolve interfaces smaller than the cell size, since information on the subgrid scale is lost. Therefore the accuracy of the interface reconstruction and the treatment of the boundary conditions (i.e. viscous stresses and surface tension forces) become grid-size-dependent. On the other hand, the FEM with deforming interface mesh allows accurate implementation of the boundary conditions, but it cannot handle large surface deformations occurring in breaking and merging of liquid regions. Combining the two methods into a hybrid FEM–VOF method eliminates the major shortcomings of both. The outcome is a technique which can handle large surface deformations with accurate treatment of the boundary conditions. For illustration, two computational examples are presented, namely the instability and break-up of a capillary jet and the coalescence collision of two liquid drops.

KEY WORDS: volume-of-fluid; free surface flows; interface advection

1. INTRODUCTION

Free surface flows and interfaces between two immiscible fluids or materials with different phases are observed in many natural and industrial processes. Various numerical techniques have been developed to simulate these flows. However, owing to the complexity of the problem, each technique is tailored to a particular category of flows. For instance, boundary integral techniques[1–3] are mainly used for simulating inviscid irrotational flows and the limiting case of zero Reynolds number. Finite element methods (FEMs) and finite difference methods (FDMs) are potentially applicable to generalized Navier–Stokes equations; however, they have to be coupled with a technique to track the advecting fluid boundaries and interfaces. The difficulty in the interface tracking is inherently related to the complexity of its topology. Therefore techniques which can handle small surface deformations fail when applied to large interface distortions. For simulation of the former category of flows (small surface deformations) the FEM is more popular. Here the fluid boundary is described by a set of fixed[4] or deforming[5–12] meshes, the location of which is obtained by either an iterative procedure or the Lagrangian movement of the interface nodes. This results in the simultaneous calculation of the position of the free surface and the field variables at the new nodal positions. Boundary-fitted orthogonal co-ordinates[13–15] and Lagrangian techniques[16,17] are also used to follow the advecting liquid interfaces. These techniques are confronted with difficulties when applied to large surface deformations, surface breaking and merging.

CCC 0271–2091/95/121363–18

Received 9 September 1993
Revised 25 August 1994

More versatile and robust techniques for free surface flow modelling are the front-tracking methods. Here an extra set of parameters is used to trace the fluid boundaries. Front-tracking techniques are divided into two groups: surface-tracking and volume-tracking methods. In general the former class gives a more accurate description of the free surface but the latter class can handle complicated liquid regions more easily. In surface-tracking methods the position of the free surface is described in a direct way, either by specifying a set of marker points located on the free surface[18] or by introducing a height function which explicitly describes the free surface position.[19] There are several problems associated with surface-tracking methods. The main problem is that the marker points will be non-uniformly distributed as the interface evolves. Also, relatively high computer storage is needed to maintain the interface continuous and smooth.

Volume-tracking techniques define a tracer to follow the whole fluid region. The two commonly used techniques are the MAC and VOF techniques. In the marker-and-cell (MAC) technique.[20–23] hundreds of massless marker particles are added to the fluid. These particles are then advected in a Lagrangian sense using the average of Eulerian velocities in their vicinity. In the volume-of-fluid (VOF) technique[24–32] a volume fraction parameter f is described for each of the Eulerian grid cells. A cell is assumed to be filled with liquid if $f = 1$, empty if $f = 0$ and partially full if $0 < f < 1$. Different methods are developed to advect the volume fraction field and to reconstruct the fluid surface. VOF-based techniques can handle the most complex free surface flow problems. Surface breaking and merging can be treated with this technique, since the flow field calculations are decoupled from the free surface location identification. Here, knowing the initial fluid surface location and the velocity field, the surface is advected using the volume fraction field, a surface is reconstructed based on the newly calculated volume fractions and finally the conservation equations are solved for the new fluid domain to find the velocity field. This procedure is repeated throughout the advection of the fluid region. There is generally no need for iteration between the flow field calculation and the interface location identification. However, presently there is a major shortcoming of these techniques. Although the interface itself can be located inside a cell, the governing equations for the field variables are only solved for the whole cell. This results in significant inaccuracies in the treatment of the interface viscous stresses and the surface tension forces.

The present paper describes a new technique for the simulation of free surface flows and interfaces by combining the FEM with deforming interface mesh and a VOF-based technique called FLAIR[31] for surface advection. The combination of these two will solve the major shortcomings of each technique. The VOF-based technique will allow the simulation of interfaces with large deformations, even with surface merging and breaking. In addition, the FEM with deforming interface mesh allows accurate implementation of the boundary conditions. In Section 2 the governing equations of free surface viscous flows are provided. Their finite element formulation is given in Section 3 and the mesh generation and advection techniques are described in Sections 4 and 5 respectively. Sections 6 and 7 provide a detailed description of the simulation of surface breaking and surface merging via two example problems. Concluding remarks are made in Section 8.

2. GOVERNING EQUATIONS

The problem considered here is the laminar flow of a viscous incompressible fluid. The assumptions of a Newtonian fluid with constant properties are also applied. Therefore the flow field is governed by the continuity and momentum (Navier–Stokes) equations

$$\frac{\partial u}{\partial z} + \frac{1}{r^\beta}\frac{\partial}{\partial r}(r^\beta v) = 0, \tag{1}$$

$$\frac{\partial u}{\partial t}+u\frac{\partial u}{\partial z}+v\frac{\partial u}{\partial r}=-\frac{\partial p}{\partial z}+\frac{1}{Re}\left[\frac{\partial^2 u}{\partial z^2}+\frac{1}{r^\beta}\frac{\partial}{\partial r}\left(r^\beta\frac{\partial u}{\partial r}\right)\right], \tag{2}$$

$$\frac{\partial v}{\partial t}+u\frac{\partial v}{\partial z}+v\frac{\partial v}{\partial r}=-\frac{\partial p}{\partial r}+\frac{1}{Re}\left[\frac{\partial^2 v}{\partial z^2}+\frac{1}{r^\beta}\frac{\partial}{\partial r}\left(r^\beta\frac{\partial v}{\partial r}\right)-\beta\frac{v}{r^2}\right], \tag{3}$$

where $\beta = 0$ for 2D Cartesian and $\beta = 1$ for axisymmetric flows. Equations (1)–(3) are written in non-dimensional form using the non-dimensional parameters

$$z=\frac{z'}{L},\qquad r=\frac{r'}{L},\qquad t=\frac{t'U}{L},$$

$$u=\frac{u'}{U},\qquad v=\frac{v'}{U},\qquad p=\frac{p'}{\rho U^2},$$

$$Re=\frac{\rho UL}{\mu},\qquad We=\frac{\rho U^2 L}{\sigma},$$

where ρ, μ and σ represent the density, viscosity and surface tension coefficient of the fluid respectively. Lengths and velocities are normalized with the characteristic scales L and U.

The boundary conditions are given by

$$\left.\begin{aligned} u&=F(z,\,r)\\ v&=G(z,\,r)\end{aligned}\right\}\quad \text{on } S_1, \tag{5}$$

$$\left.\begin{aligned} \bar\tau_{zz}&=\frac{\bar\tau'_{z'z'}}{\rho U^2}=\left(\frac{2}{Re}\frac{\partial u}{\partial z}-p\right)n_z+\frac{1}{Re}\left(\frac{\partial u}{\partial r}+\frac{\partial v}{\partial z}\right)n_r\\ \bar\tau_{rr}&=\frac{\bar\tau'_{r'r'}}{\rho U^2}=\frac{1}{Re}\left(\frac{\partial u}{\partial r}+\frac{\partial v}{\partial z}\right)n_z+\left(\frac{2}{Re}\frac{\partial v}{\partial r}-p\right)n_r\end{aligned}\right\}\quad \text{on } S_2, \tag{5}$$

where S_1 and S_2 are the parts of the boundary with Dirichlet and Neumann boundary conditions respectively, $\bar\tau_{zz}$ and $\bar\tau_{rr}$ denote the z- and r-components of the total surface traction and n_z and n_r denote the direction cosines of the unit outer normal to the surface S_2. On the free surface, $\bar\tau_{zz}$ and $\bar\tau_{rr}$ are the components of the surface tension, which is inversely proportional to the radius of curvature of the surface, R'_c:

$$\bar\tau_{zz}=\frac{\sigma/R'_c}{\rho U^2}n_z=\frac{1}{We}\frac{1}{R_c}n_z,\qquad \bar\tau_{rr}=\frac{\sigma/R'_c}{\rho U^2}n_r=\frac{1}{We}\frac{1}{R_c}n_r. \tag{6}$$

The non-dimensional radius of curvature of an axisymmetric surface is defined as

$$\frac{1}{R_c}=\frac{1}{R_1}+\frac{1}{R_2},$$

with R_1 and R_2, * being the principal radii of curvature of the surface, defined as

$$R_1=\frac{[1+(\mathrm{d}r/\mathrm{d}z)^2]^{1\cdot5}}{\mathrm{d}^2r/\mathrm{d}z^2},\qquad R_2=r\left[1+\left(\frac{\mathrm{d}r}{\mathrm{d}z}\right)^2\right]^{0\cdot5}.$$

No contact between the fluid and the solid surface is involved in the problems considered in this paper, so the contact angle is not modelled here.

* For a two-dimensional surface, $R_2=\infty$.

3. FINITE ELEMENT FORMULATION

The selection of the finite element solution to the conservation equations (1)–(3) is subject to two major restrictions. First, because of the requirements of the advection technique, which is basically designed for finite difference schemes, the finite element solution should be in terms of primitive variables based on the linear quadrilateral elements. Furthermore, owing to the significance of the surface tension effects in free surface flows, the model must be capable of handling the pressure, velocity, velocity gradient and stress boundary conditions directly.

A finite element model which complies with these requirements is the penalty function formulation, in which the continuity equation is absorbed in the momentum equation by representing the pressure as

$$p = -\lambda\left(\frac{\partial u}{\partial z} + \frac{1}{r^{\beta}}\frac{\partial}{\partial r}(r^{\beta}v)\right), \tag{7}$$

where λ ($O(10^9)$) is a large number depending on μ and Re^{33}. Substituting the pressure equation (7) into the momentum equations (2) and (3) and applying the Galerkin method, the following matrix equations are obtained:

$$\begin{pmatrix} [M] & [0] \\ [0] & [M] \end{pmatrix}\begin{pmatrix} \{\dot{u}\} \\ \{\dot{v}\} \end{pmatrix} + \begin{pmatrix} [C_{11}]+[C_{22}] & [0] \\ [0] & [C_{11}]+[C_{22}] \end{pmatrix}\begin{pmatrix} \{u\} \\ \{v\} \end{pmatrix}$$

$$+\frac{1}{Re}\begin{pmatrix} 2[K_{11}]+[K_{22}] & [K_{12}] \\ [K_{12}]^{\mathrm{T}} & [K_{11}]+2[K_{22}]+\beta 2[K_{33}] \end{pmatrix}\begin{pmatrix} \{u\} \\ \{v\} \end{pmatrix}$$

$$+\frac{\lambda}{\mu Re}\begin{pmatrix} [L_{11}] & [L_{12}]+\beta[L_{13}] \\ [L_{12}]^{\mathrm{T}}+\beta[L_{13}]^{\mathrm{T}} & [L_{22}]+\beta([L_{23}]+[L_{23}]^{\mathrm{T}}+[L_{33}]) \end{pmatrix}\begin{pmatrix} \{u\} \\ \{v\} \end{pmatrix} = \begin{pmatrix} \{R_u\} \\ \{R_v\} \end{pmatrix}. \tag{8}$$

Here

$$[M] = \int_{\Omega^e} N_i N_j \, \mathrm{d}\Omega, \tag{9}$$

$$[C_{11}] = \int_{\Omega^e} u_{\mathrm{n}} N_i \frac{\partial N_j}{\partial z}\, \mathrm{d}\Omega, \qquad [C_{22}] = \int_{\Omega^e} v_{\mathrm{n}} N_i \frac{\partial N_j}{\partial r}\, \mathrm{d}\Omega, \tag{10}$$

$$[K_{11}] = \int_{\Omega^e} \frac{\partial N_i}{\partial z}\frac{\partial N_j}{\partial z}\, \mathrm{d}\Omega, \qquad [K_{12}] = \int_{\Omega^e} \frac{\partial N_i}{\partial r}\frac{\partial N_j}{\partial z}\, \mathrm{d}\Omega, \tag{11}$$

$$[K_{22}] = \int_{\Omega^e} \frac{\partial N_i}{\partial r}\frac{\partial N_j}{\partial r}\, \mathrm{d}\Omega, \qquad [K_{33}] = \int_{\Omega^e} \frac{1}{(r^{\beta})^2} N_i N_j \mathrm{d}\Omega, \tag{12}$$

$$[L_{11}] = \int_{\Omega^e} \frac{\partial N_i}{\partial z}\frac{\partial N_j}{\partial z}\, \mathrm{d}\Omega, \qquad [L_{12}] = \int_{\Omega^e} \frac{\partial N_i}{\partial z}\frac{\partial N_j}{\partial r}\, \mathrm{d}\Omega, \tag{13}$$

$$[L_{22}] = \int_{\Omega^e} \frac{\partial N_i}{\partial r}\frac{\partial N_j}{\partial r}\, \mathrm{d}\Omega, \qquad [L_{13}] = \int_{\Omega^e} \frac{1}{r^{\beta}}\frac{\partial N_i N_j}{\partial z}\, \mathrm{d}\Omega, \tag{14}$$

$$[L_{23}] = \int_{\Omega^e} \frac{1}{r^\beta} \frac{\partial N_i}{\partial r} N_j \, d\Omega, \qquad [L_{33}] = \int_{\Omega^e} \frac{1}{(r^\beta)^2} N_i N_j \, d\Omega, \tag{15}$$

$$\{R_u\} = \int_\Gamma \bar{\tau}_{zz} N_i^* \, d\Gamma, \qquad \{R_v\} \int_\Gamma \bar{\tau}_{rr} N_i^* \, d\Gamma, \tag{16}$$

where the N_i are the shape functions for the isoparametric quadrilateral elements in the domain Ω with boundary Γ. Integrals (9)–(12) and (16) are evaluated by the 2×2 Gauss–Legendre integration rule. The $[L]$-matrix should be singular for the penalty function approach to be successful. A reduced Gauss integration is used to evaluate the $[L]$-matrix given by integrals (13)–(15). The surface traction resulting from the surface tension effects is directly integrable over the free surface using equation (16). Equation (8) is integrated in time using an implicit forward-differencing finite difference technique.

4. MESH GENERATION

Mesh generation for a finite element problem has proven to be an important part of the overall solution procedure. A large effort is devoted to this issue in order to generate the most efficient mesh for every particular problem, using various techniques such as Laplace's equation[34] and transfinite mapping.[35–37] These techniques generate the interior nodes based on the predefined boundary nodes and in general there is no control on the location of the generated interior nodes. In the case of highly distorted domains it is necessary to divide the whole domain into simple subdomains. However, where moving boundaries are involved, the solution domain experiences successive evolutions in the course of time, resulting in the redefinition of subdomains. This can be tedious for very complicated boundary evolutions such as the cases encountered in breaking or merging of two liquid regions. These limitations along with the requirements of the advection technique for moving interfaces make the use of automatic mesh generators inconvenient.

In the present work a rectangular finite element mesh is used in order to utilize the existing interface advection techniques. Implementation of the finite element method on the Eulerian grid for solving moving boundary problems is well developed[4,38] and can be applied to the present model. In order to describe the mesh generation method used in this work, consider the closed curve located on the Eulerian grid shown in Figure 1. The master element chosen for the finite element mesh is the isoparametric linear quadrilateral element, which is also suitable for the penalty function method used

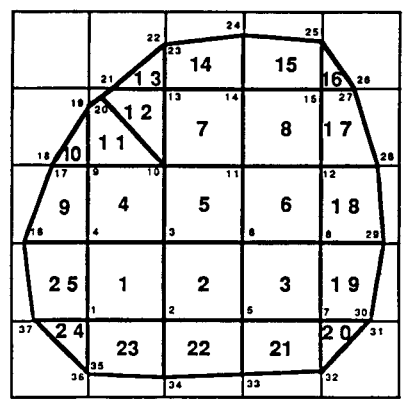

Figure 1. Finite element mesh numbering in the Eulerian grid. The bold numbers are element numbers and the smaller numbers are node numbers

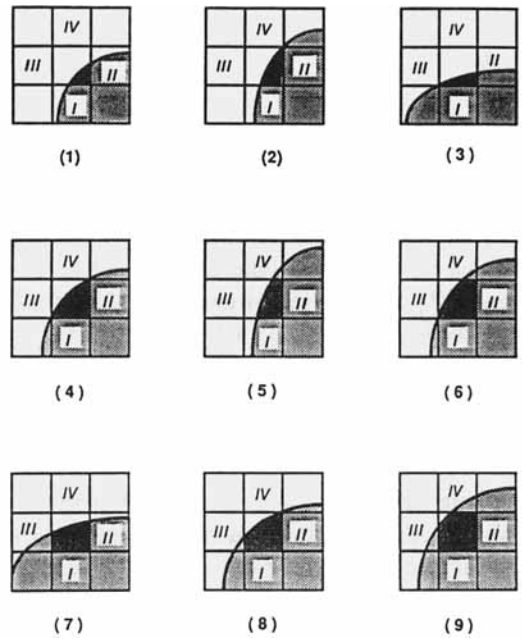

Figure 2. Different cases for the wet cell regarding the intersection points of the interface with the cell faces

in the momentum solver. Hence each full cell will be considered as one element and we begin numbering the elements with the first full cell located on the left of the lowest row, then continuing towards the full cells on the right of this cell and repeating the same procedure for the other rows. The intersecting points of grid lines are the nodes and they are numbered counterclockwise for each element, starting from the lower left node, as shown in Figure 1.

Once the full cells have been completely transformed into elements, the wet cells must be employed to define the rest of the mesh. Depending on the intersection points of the interface line with the faces of the cell, nine possible cases for a wet cell can be recognized. These cases are shown in Figure 2, with the wet cell located at the centre of a 3×3 cell unit. Note that the unit is first rotated so that the heavy side (the side which contains more mass than the other three sides) is on the lower right corner as shown in Figure 2. These cases can be distinguished by examining the four cells located on the middle of each side of the unit, namely cells I–IV as shown in Figure 2. All possible cases are summarized in Table I. In cases (5)–(8) of Figure 2 the four nodes are well defined, while in cases (1)–(4) a fourth node has to be defined between the two interface nodes. Case (9) includes five nodes and cannot be considered as one element. Therefore an extra node is defined between the two nodes which are located on the free surface. This transforms the wet cell into two elements.

The above procedure may result in very small elements on the free surface adjacent to larger rectangular elements. These small elements are encountered when the free surface crosses an interface cell very close to its interior node(s) as seen in Figure 3(a). Therefore the mesh should be altered in this region to redefine the spacing between the nodes. This can be accomplished by moving the interior nodes of the surface cells away from the interface. Figure 3(b) shows the altered mesh, which now has a better aspect ratio for the surface elements. The inward displacement of the interior node is proportional to its distance from the interface: the closer the node is to the interface, the more it is displaced.

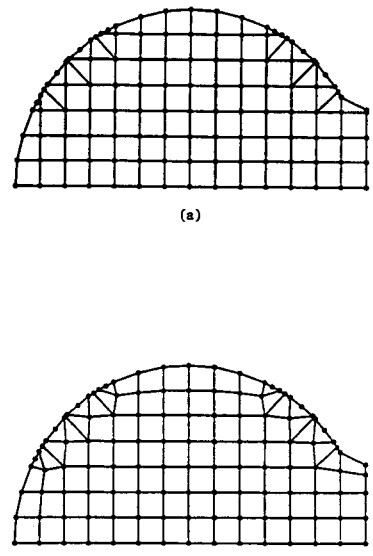

Figure 3. The mesh containing small elements (a) is altered by displacing the interior nodes of the surface cells (b)

Table I. Case-distinguishing criteria for wet cells shown in Figure 2

Case	Cell I	Cell II	Cell III	Cell IV
(1)	Wet	Wet	Empty	Empty
(2)	Wet	Full	Empty	Empty
(3)	Full	Wet	Empty	Empty
(4)	Full	Full	Empty	Empty
(5)	Wet	Full	Empty	Wet
(6)	Full	Full	Empty	Wet
(7)	Full	Wet	Wet	Empty
(8)	Full	Full	Wet	Empty
(9)	Full	Full	Wet	Wet

5. SURFACE ADVECTION

Once the velocities have been obtained, the interface has to be advected. We have implemented the flux line segment model for advection and interface reconstruction (FLAIR) originally developed by Ashgriz and Poo[31] for 2D Cartesian advection and later extended by Mashayek and Ashgriz[32] to Axisymmetric flows. In this technique a volume fraction $f_{i,j}$ is defined for each cell such that $f_{i,j} = 1$ for cells which are filled with liquid, $f_{i,j} = 0$ for empty cells and $0 < f_{i,j} < 1$ for interface or wet cells. Therefore the liquid domain is discretized and represented by a set of volume fractions which we will refer to as the f-field. The FLAIR technique is designed to advect the f-field by knowing the surface velocities and to reconstruct the surface topology based on the new f-field.

The principle of surface advection by FLAIR is illustrated in Figure 4. It is assumed that the surface can be represented by a set of line segments drawn at the boundary of two neighbouring cells.

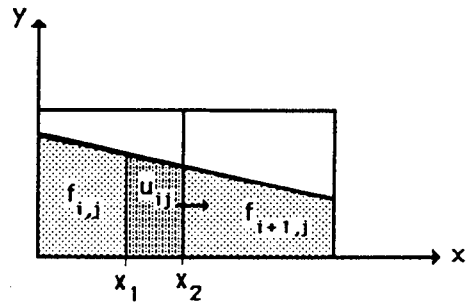

Figure 4. Interface advection method for two neighbouring cells by FLAIR technique

Therefore each line segment can be described by $y = ax + b$, where the constants a and b can be determined based on the known volume fractions[31] $f_{i,j}$ and $f_{i,j+1}$. Once the surface has been reconstructed by the combination of all surface line segments, it is advected by calculating the mass flux in and out of each cell. The mass flux in each time step δt moving from one cell to the neighbouring cell can be calculated by using the velocity at the boundary of the two cells, $u_{i,j}$, as

$$\delta f = \int_{x_1}^{x_2} y \, dx = \tfrac{1}{2}a(x_2^2 - x_1^2) + b(x_2 - x_1).$$

Here $x_2 - x_1$ represents the distance the mass is advected in time δt, i.e. $x_2 - x_1 = u_{i,j}\delta t$. Therefore the mass flux in time step δt for a surface with the orientation shown in Figure 4 and $x_2 = 1$ is

$$\delta f = u_{i,j}\delta t(a + b - \tfrac{1}{2}au_{i,j}\delta t).$$

Other surface orientations and advection in the vertical direction can be considered in a similar fashion.[31,32] The new cell volume fraction is then obtained by adding the old value to the net influx of the volume fraction to each cell.

This advection technique has been basically designed for the finite difference staggered grids where the velocities are defined at the middle of each cell face. However, finite element solution of the flow provides the velocities at the nodes of the element, which are not suitable for this advection technique. Mashayek and Ashgriz[32] have shown that the advection criterion can be deduced from satisfying the continuity of the flow through the faces of each cell during every time step. We use the same idea and calculate a mean velocity from the known velocities at the two nodes attached to the ends of one cell face such that the same mass of fluid passes through that face.

Consider the axial direction in an axisymmetric flow. Each cell in the r–z plane is mapped into an isoparametric master element in the ξ–η plane as shown in Figure 5. The mean velocity $\bar{u}_{23}$ across the face 2–3 is defined by

$$\bar{u}_{23} \int_{\Gamma_{23}} \Gamma = \int_{\Gamma_{23}} u \, d\Gamma, \tag{17}$$

where the velocity and radius are defined as

$$u = u_i N_i, \qquad r = r_i N_i, \tag{18}$$

with the N_i being the shape functions for the isoparametric quadrilateral elements, defined as

$$N_1(\xi, \eta) = \tfrac{1}{4}(\xi - 1)(\eta - 1), \qquad N_2(\xi, \eta) = -\tfrac{1}{4}(\xi + 1)(\eta - 1),$$
$$N_3(\xi, \eta) = \tfrac{1}{4}(\xi + 1)(\eta + 1), \qquad N_4(\xi, \eta) = -\tfrac{1}{4}(\xi - 1)(\eta + 1). \tag{19}$$

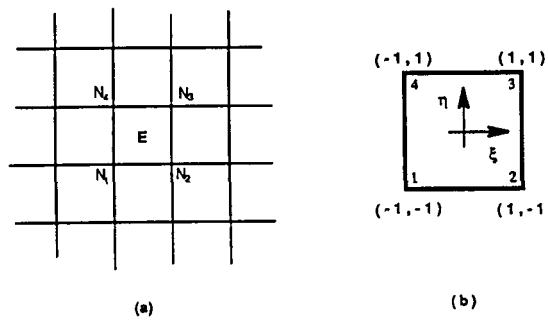

Figure 5. Mapping of the Eulerian element (a) into the master isoparametric element (b)

Then

$$\int_{\Gamma_{23}} u \, d\Gamma = \int_{\Gamma_{23}} 2\pi u r \, dr = 2\pi \int_{\Gamma_{23}} (u_i N_i)(r_j N_j)\left(\frac{\partial r}{\partial \xi} d\xi + \frac{\partial r}{\partial \eta} d\eta\right).$$

The side 2–3 of the cell is mapped onto the side 2–3 of the master element where $\xi = 1$ and $d\xi = 0$. Therefore

$$\int_{\Gamma_{23}} u \, d\Gamma = 2\pi \int_{-1}^{1} (u_2 N_2 + u_3 N_3)(r_2 N_2 + r_3 N_3)\left(r_2 \frac{\partial N_2}{\partial \eta} + r_3 \frac{\partial N_3}{\eta}\right) d\eta.$$

After substituting for N_2, N_3 and their derivatives, we find that

$$\int_{\Gamma_{23}} u \, d\Gamma = \frac{\pi}{3}(r_3 - r_2)(2r_3 u_3 + r_2 u_3 + r_3 u_2 + 2r_2 u_2). \tag{20}$$

The integral on the left-hand side of equation (17) can be written as

$$\int_{\Gamma_{23}} d\Gamma = \pi(r_3^2 - r_2^2). \tag{21}$$

Combining equations (17), (20) and (21) gives

$$\bar{u}_{23} = \frac{2r_2 u_3 + r_2 u_3 + r_3 u_2 + 2r_2 u_2}{3(r_3 + r_2)}. \tag{22}$$

Applying the same analysis in the radial direction shows that $\bar{v}$ is just the average of the v-velocities at the ends of the cell face:

$$\bar{v}_{34} = \tfrac{1}{2}(v_3 + v_4). \tag{23}$$

In order to clarify the connection between the various steps employed in the FEM–VOF technique, consider the oscillation of a liquid drop as shown in Figure 6. Owing to the symmetry, a quarter of the drop, as depicted by the shaded area in Figure 6(a), is analysed. By assigning a value of the volume fraction f to every cell, this area is converted to a set of numbers as shown in Figure 6(b). The interface shown in Figure 6(c) is reconstructed based on this f-field by using the FLAIR algorithm.[31,32] Then, by implementing the method explained in Section 4, the FEM mesh is generated as shown in Figure 6(d) with thick lines. After the momentum equations have been solved, the velocities are obtained at the nodal points of the mesh. These velocities, which are shown in Figure 6(e), are then transformed to the velocity field depicted in Figure 6(f) by applying equations (22) and (23). In the next step the new

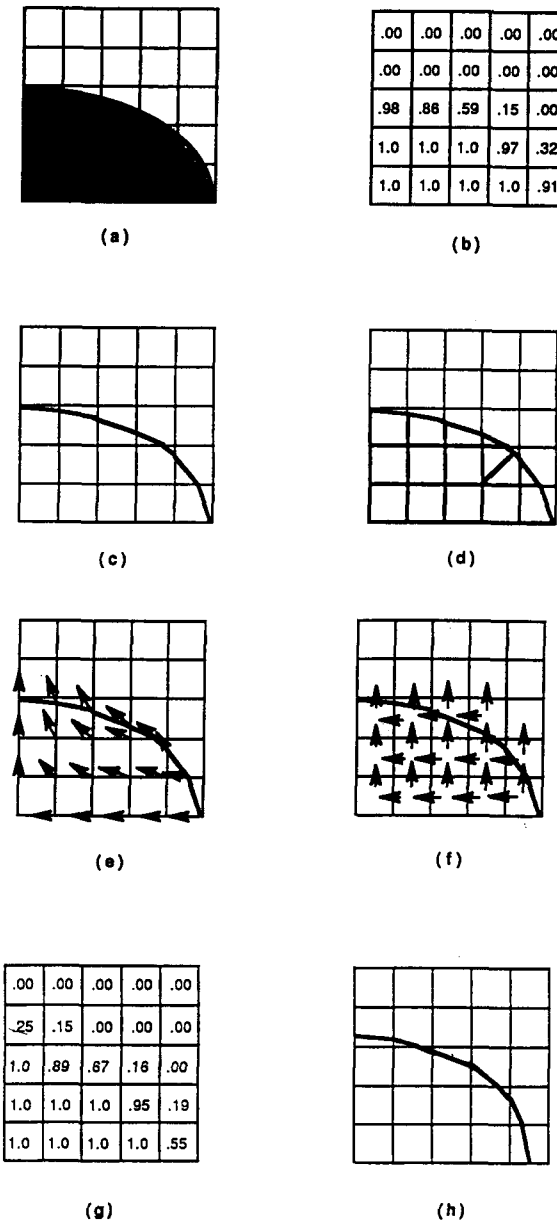

Figure 6. Illustration of the steps taken in FEM–VOF: (a) definition of the initial interface; (b) description of the f-field; (c) reconstruction of the interface based on the f-field; (d) mesh generation; (e) calculation of the velocity field by FEM; (f) calculation of the velocities at the cell faces; (g) advection of the liquid and calculation of the new f-field based on FLAIR; (h) reconstruction of the new interface

f-field is obtained through advecting the old f-field by implementing FLAIR. The new f-field is shown in Figure 6(g) and is used to reconstruct the new interface depicted in Figure 6(h). This will complete the sequences employed in the first time step and in continuation the steps of Figures 6(d)–6(h) will be repeated for each time step.

The FEM along with the VOF method for interface advection has several important advantages. The first advantage of FEM–VOF is in modelling surface breaking and merging. In fluid regions where surface breaking or merging is about to occur, the accuracy of the solution can be greatly enhanced if very small fluid thicknesses at the break-up point or very small distances between the two merging surfaces are considered. This can be easily achieved by the FEM–VOF method, since the interface boundary condition can be applied accurately. The previous VOF techniques combined with the finite difference method (FDM–VOF) have to resort to an interpolation technique for implementation of the interface boundary conditions. Since the liquid surface is continuously moving, new cells are being formed. Therefore, in order to complete the boundary conditions needed for the momentum equations, new velocity components have to be defined for the newly formed interface cells. This is achieved by applying the continuity equation to these interface cells.[31] In many of the VOF techniques, when the thickness of the liquid comes within the order of one cell size, this method fails, since it results in double definition of the boundary velocities. Therefore the criterion for liquid break-up is set to be when the local liquid thickness reaches one cell size.

Another advantage of FEM–VOF over FDM–VOF is that the former defines a computational element for the part of the wet cell which actually contains fluid, while in FDM–VOF the wet cells are treated in the same way as the full cells using the whole rectangular cell for the discretization of the momentum equation. This allows accurate calculation of the boundary conditions without resorting to time-consuming interpolations as in FDM–VOF. By implementing the FEM in the momentum solver, this technique is capable of handling the pressure and velocity boundary conditions accurately. The techniques based on the FDM are incapable of applying these boundary conditions directly. In the most recent improvements presented by Unverdi and Tryggvason[39] and Brackbill *et al.*,[40] the surface tension effects are considered as a body force distributed in the cells close to the interface. This may result in large errors when the thickness of the fluid is small, which is unavoidable in breaking and merging of liquids. In the present technique the interface is treated as a discontinuity, which has better resolution in comparison with the techniques that smear the interface over some finite region.

Finally, FEM–VOF significantly increases the computational efficiency, because a smaller number of cells will be sufficient to model large surface deformations. The number of cells in each direction used in this technique is 2·5 times smaller than that required in the FDM–VOF technique of Ashgriz and Poo[31] in order to have the same accuracy. The problem of area change reported by Ashgriz and Poo[31] is almost completely resolved by keeping the divergence of the velocity less than 10^{-9} for each element in each time step. The momentum solver is fully implicit and therefore imposes no significant limit on the selection of the time increment. Consequently, the time increment will be determined by the advection technique, which is less restricted than the common explicit or semi-implicit momentum solvers. This will result in a substantial decrease in the total number of time steps and will increase the overall efficiency and accuracy of the method.

6. SURFACE BREAKING

As mentioned earlier, in FEM–VOF the continuous movement of the interface line inside a wet cell results in the formation of different elements at different time steps. There is no limit on the size of these elements, so the thickness of the liquid can be reduced to a small fraction of the cell size. The advantage of this capability is illustrated by the surface movement of an unstable capillary jet as shown in Figure 7. The initially disturbed surface is indicated in Figure 7(a). We have used two cells for the initial radius and 16 cells for one wavelength of the jet. Implementing the FEM–VOF technique allows us to accurately decrease the thickness of the jet as much as desired. For instance, the curve depicted in Figure 7(c) shows the jet surface which has a minimum radius of about 5% of the undisturbed initial jet radius. This technique is implemented to simulate the break-up of a capillary jet.

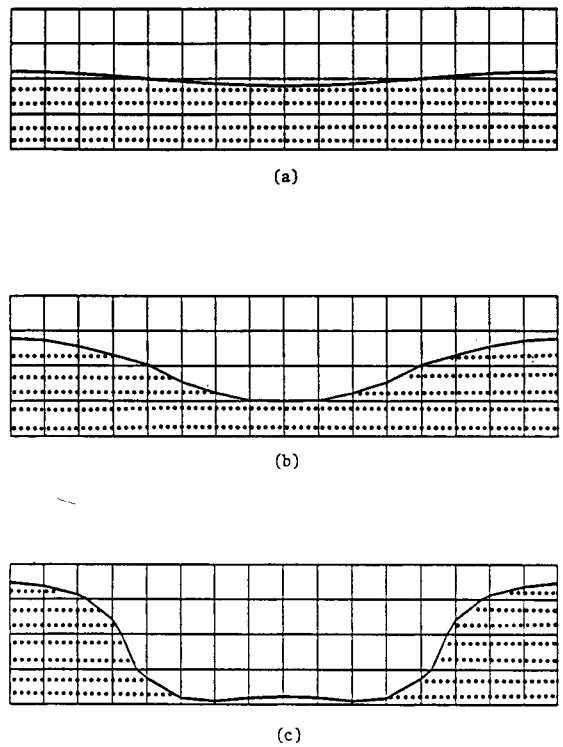

Figure 7. Computational model for the break-up of a liquid jet: (a) initial disturbed surface; (b) surface location at the break-up limit for FDM–VOF; (c) surface location at the break-up limit for FEM–VOF

Rayleigh,[41] for the first time, obtained a linear analytical solution for the instability of inviscid jets in vacuum. Later the analytical analysis was extended to non-linear inviscid jets by Yuen[42] and linear viscous jets by Chandrasekhar.[43] However, the non-linear instability of viscous jets has not been the subject of analytical investigations. The experimental and numerical studies cover a broader range and are reported by a large number of researchers, such as the works done experimentally by Goedde and Yuen[44] and Vassallo and Ashgriz[45] and numerically by Mansour and Lundgren.[46]

As a test problem for the FEM–VOF technique we have considered the break-up of an infinitely long jet in vacuum, subject to a periodic surface disturbance in the form of

$$r(z) = 1 + \eta \cos(kz),$$

where η and k are the amplitude and wave number respectively. The undisturbed radius of the jet is selected as the length scale, while the time scale is obtained by equating the Weber number to unity. In order to validate the results, we consider the break-up of a glycerin–water jet with $k = 0{\cdot}262$ and $Re = 2{\cdot}045$, which has been experimentally studied by Goedde and Yuen.[44] The results of our solution with $\eta_0 = 0{\cdot}02$ are shown in Figure 8 in different snapshots. Initially, the jet begins to swell at $z = \pm 12{\cdot}0$ and necks down at $z = 0$. However, after a short time interval the point having minimum radius starts moving towards the points $z = \pm 12{\cdot}0$. Finally the jet breaks at $z \approx \pm 9{\cdot}0$, leaving a spherical drop and a cylindrical ligament.

Figure 9(a) shows the variation in the amplitude of the swell and neck regions of the jet with time. The non-linear effects are clearly seen close to the break-up point, where the amplitude of the swell

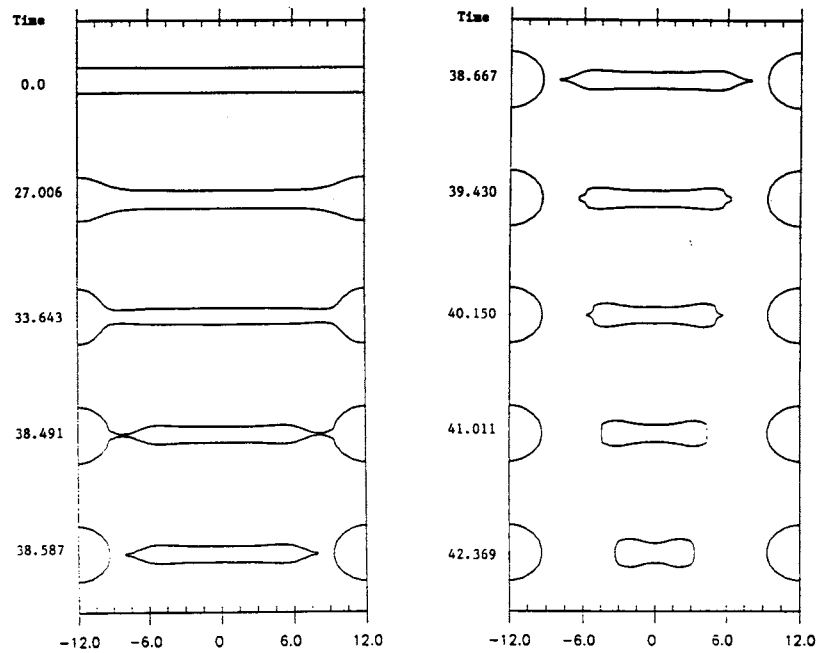

Figure 8. Time-resolved simulation of the break-up of a liquid jet: $Re = 2{\cdot}045$, $We = 1$, disturbance wave number $k = 0{\cdot}262$

region becomes flat and the neck region reduces rapidly. To evaluate the accuracy of the calculations, we have compared our numerically calculated growth rates with Goedde and Yuen's[44] experimental data and Chandrasekhar's[43] analytical results.

The same procedure as used by Goedde and Yuen[44] for the calculation of the growth rates from the experimental data is also used here. The exponential growth rate ω is defined by $\eta = \eta_0 e^{\omega t}$, where η is the wave amplitude with the value of η_0 at $t = 0$. Then

$$\omega = \frac{1}{t} \ln\left(\frac{\eta}{\eta_0}\right).$$

Therefore ω is the slope of the curve $\ln(\eta/\eta_0)$ versus time when this curve is approximated by a line. We have observed the same variation in the growth rate as reported by Goedde and Yuen.[44] The exponential growth rate is not constant at any particular point of the jet surface, but the exponential growth rate of the difference between the swell and the neck is nearly constant (except close to the break-up point) as shown in Figure 9(b). The numerically calculated average growth rate for the swell point is $\omega_s = 0{\cdot}153$ and for the neck point is $\omega_n = 0{\cdot}107$. The growth rate for the difference between the amplitude of the swell and neck points is $\omega = 0{\cdot}131$. The analytically calculated growth rate for a viscous jet[43] for the same Re is $\omega_a = 0{\cdot}134$. Goedde and Yuen's[44] experiments under approximately the same conditions resulted in a growth rate of $\omega_e = 0{\cdot}118$. Considering the experimental error, which was estimated[44] to be about 11%, the coarse numerical mesh used in our simulation and that the initial disturbance amplitudes are not the same (initial disturbance amplitudes for the experimental results are not reported), the observed differences between the experimental and numerical results are acceptable.

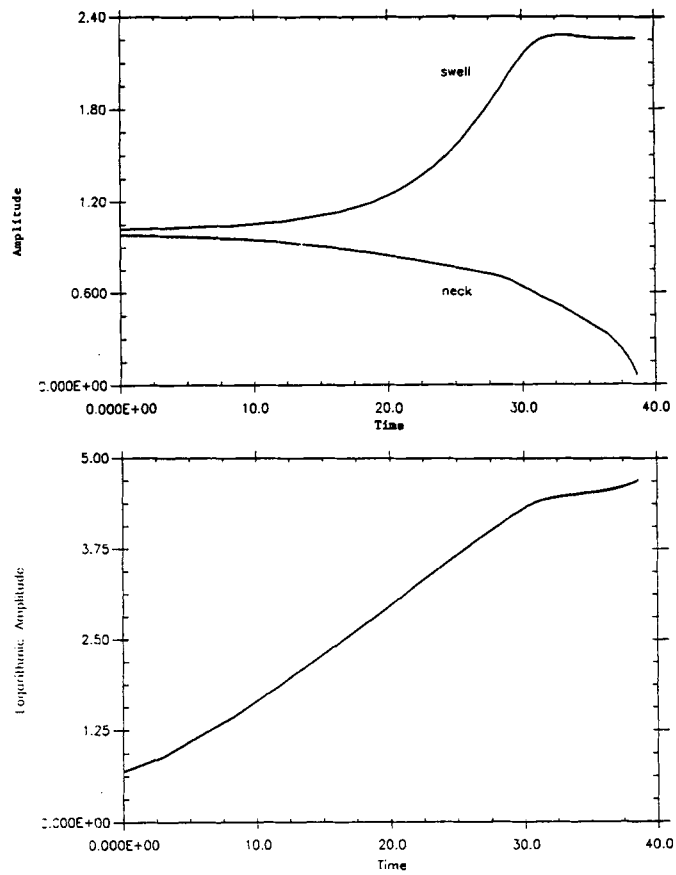

Figure 9. (a) Variation in swell point and neck point amplitudes with time. Amplitude and time are both non-dimensionalized. (b) Logarithmic plot of amplitude difference between swell and neck points corresponding to Figure 8

7. SURFACE MERGING

The ability to accurately implement the boundary condition becomes more physically attractive when the collision of two liquid drops in non-vacuum surroundings is involved. In this case the fluid trapped between the drops prevents merging and flat regions are developed on the surface of the drops which are about to collide. The thickness of the fluid between the drops is decreased owing to the pressure generated by the drops and merging becomes possible if the initial momentum of the drops is capable of producing a pressure high enough to rupture the trapped liquid film, otherwise the drops are bounced apart. In a real collision process the thickness of the film may be reduced to a level comparable with molecular size and still the merging be prevented. Therefore the margin of bouncing/merging collisions is not accurately found by implementing techniques that model the merging phenomenon at the level of cell size.

The complex problem of the collision of two viscous liquid drops is chosen to demonstrate the capability of the FEM–VOF method in handling the merging of two liquid surfaces. Because of the complexity of this problem, the majority of the published literature in this area has been limited to experimental research—Ashgriz and Poo[47] provide a detailed count of the previous works in this field

up to 1990. Limited numerical simulations have been attempted by Poo and Ashgriz[48] using the FLAIR algorithm. However, their simulation was for the collision of two liquid cylinders or two-dimensional drops.

Here we present the binary collision of 3D drops in axisymmetric co-ordinates. This will limit us to only head-on collisions. Figures 10(a)–10(h) show the time evolution of the collision of two drops with $Re = 50$ and $We = 10$—Re and We are evaluated based on the initial drop diameter and the relative velocity between the two drops, which is equal to 6 for the present calculations. The initial condition is shown in Figure 10(a), where only two elements—one on each side of the axis of symmetry—are set to touch. This condition is not necessary and the drops could be allowed to travel towards each other from a finite distance. The velocity vector on each node is plotted in all figures to show the flow field and indicate the number of elements in the system. The sizes of the vectors are scaled relative to the initial velocity and the ratio is given as x. Note that the number of elements can change as it has in Figure 10(b).

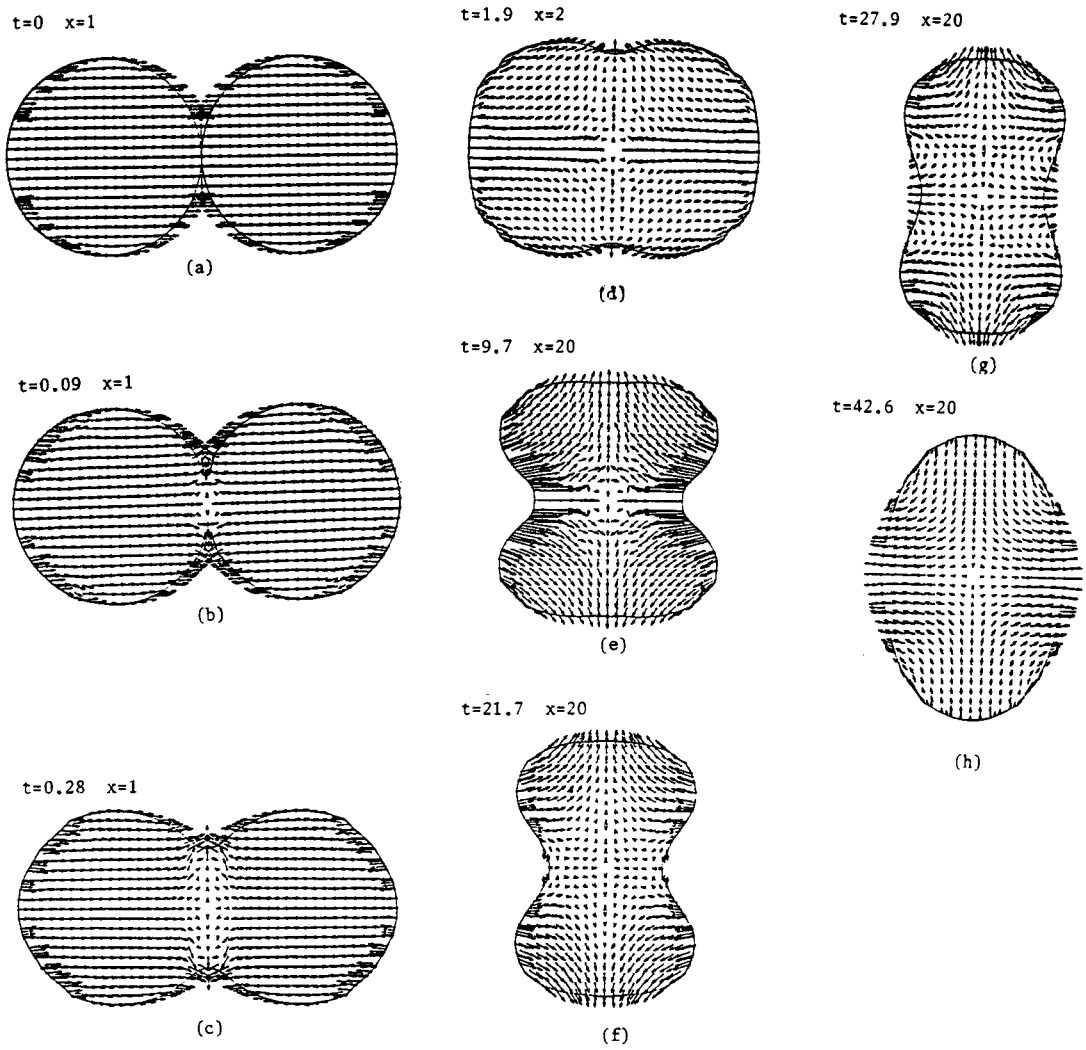

Figure 10. Collision dynamics of two liquid drops: $Re = 30$, $We = 50$

A very interesting transient flow field is observed during the collision of the two drops. Shortly after the collision ($t = 0{\cdot}09$, Figure 10(b)) the flow at the back side of each drop slows down, while the top and bottom sides of the drops continue their motions. This results in the eventual formation of the shape shown in Figure 10(d). At the collision surface the stagnation-type flow pushes the interface to the sides, generating a combined drop as shown in Figure 10(f). The inertia forces keep pushing the liquid to the sides and the surface of the drop moves inwards around the axis of symmetry as seen in Figure 10(e). Therefore the surface tension forces are no longer in favour of pushing the liquid away from the axis. The maximum inward displacement of the surface is reached in the situation shown in Figure 10(f), which indicates the initiation of backward flow along the axis. The region covered by the reversed flow expands towards the sides of the drop (Figure 10(g)) until finally surface tension and viscous forces overcome the initial momentum of the drop and the fluid flow is completely reversed. The drop tends to become spherical with identical curvature everywhere along the boundary. Without the viscous effects the drop will oscillate infinitely; however, the presence of viscosity will finally bring it to rest. Competition between surface tension and viscosity during the intermediate stages of drop deformation may result in various modes of oscillations.

There are no reported experiments on low-*Re* drop collision with which to compare the numerical results. The Reynolds numbers for the water drop collisions of Ashgriz and Poo[47] are an order of magnitude larger than the ones reported here and could not be simulated. However, qualitative comparisons show the same evolutionary process. The two examples presented here use a very coarse mesh, which results in some surface roughness. The mesh size is kept large to show the actual interface lines and also the versatility of the method. The surfaces can be made smooth by reducing the mesh size.

8. CONCLUDING REMARKS

A new technique is developed for simulating free surface flows with large deformations. The finite element method (FEM) is used to solve the flow equations and a volume-of-fluid (VOF) technique is implemented for surface determination and interface advection. Linking between FEM and VOF is provided by developing a new mesh generation technique. Detailed comparison with finite-difference-based VOF techniques is carried out by considering two of the most commonly encountered problems in free surface flows, namely liquid breaking and merging. Compared with other FEM techniques currently used for simulating free surface flows, FEM–VOF may be less accurate, but the other FEM techniques have difficulty in modelling the break-up and merging of liquids during a single flow simulation.

To the best of our knowledge, this work represents the first attempt to combine the finite element method with a volume-of-fluid technique. Therefore modifications are still expected to be made in order to improve the versatility and applicability of the technique. The Mesh generation, for instance, can be modified to obtain a more efficient mesh by providing better aspect ratios for the surface elements. Also, the loss of accuracy due to the velocity interpolations might be decreased by developing a new advection technique that utilizes nodal velocities rather than facial velocities.

REFERENCES

1. R. W. Yeung, 'Numerical methods in free surface flows', *Ann. Rev. Fluid Mech.*, **14**, 395 (1982).
2. A. S. Geller, S. H. Lee and L. G. Leal, 'The creeping motion of a spherical particle normal to a deformable interface', *J. Fluid Mech.*, **169**, 27 (1986).
3. J. M. Rallison and A. Acrivos, 'A numerical study of the deformation and burst of a viscous drop in an extensional flow', *J. Fluid Mech.*, **89**, 191 (1978).
4. K. J. Bathe and M. R. Khoshgoftaar, 'Finite element free surface seepage analysis without mesh iteration', *Int. j. numer. anal. mech. geomech.*, **3**, 13 (1979).
5. R. I. Tanner, R. E. Nickell and R. W. Bilger, 'Finite element methods for the solution of some incompressible non-Newtonian fluid mechanics problems with free surfaces', *Comput. Methods Appl. Mech. Eng.*, **6**, 155, 1975.

6. H. Saito and L. E. Scriven, 'Study of coating flow by the finite element method', *J. Comput. Phys.*, **42**, 53 (1981).
7. H. Ettouney and R. A. Brown, 'Finite element method for steady solidification problems', *J. Comput. Phys.*, **49**, 118 (1983).
8. R. Bonnerot and P. Jamet, 'Numerical computation of the free boundary for the two-dimensional Stefan problem by space–time finite element', *J. Comput. Phys.*, **25**, 163 (1977).
9. D. R. Lynch, 'Unified approach to simulation on deforming elements with application to phase change problems;, *J. Comput. Phys.*, **47**, 387 (1982).
10. P. Bach and O. Hassager, 'An algorithm for the use of the Lagrangian specification in Newtonian fluid mechanics and applications to free surface flow', *J. Fluid Mech.*, **152**, 173 (1985).
11. M. S. Sadeghipour and F. Mashayek, 'A finite element analysis of the transient freezing of liquids flowing inside tubes', *Proc. Nat. Heat Transfer Conf.*, HTD Vol. 109, 1989.
12. M. S. Engelman and R. L. Sani, 'Finite element simulation of incompressible fluid flows with a free/moving surface', *Recent Adv. Numer. Methods Fluids*, **5**, 47 (1986).
13. I. S. Kang and L. G. Leal, 'Numerical solution of axisymmetric, unsteady free-boundary problems at finite Reynolds number. 1. Finite-difference scheme and its application to the deformation of a bubble in a uniaxial straining flow', *Phys. Fluids*, **30**, 1929 (1987).
14. G. Ryskin and L. G. Leal, 'Numerical solution of the free boundary problems in fluid mechanics. Part 1. The finite-difference technique', *J. Fluid Mech.*, **148**, 1 (1984).
15. N. S. Asaithambi, 'Computation of free surface flows', *J. Comput. Phys.*, **73**, 380 (1987).
16. D. E. Fyfe, E. S. Oran and M. J. Fritts, *Naval Research Laboratory Memorandum Report 6185*, 1988.
17. M. J. Fritts and J. P. Boris, 'The Lagrangian solution of transient problems in hydrodynamics using a triangular grid', *J. Comput. Phys.*, **31**, 173 (1979).
18. I.-L. Chern, J. Glimm, O. McBryan, B. Plohr and S. Yaniv, 'Front tracking for gas dynamics', *J. Comput. Phys.*, **62**, 83–110 (1986).
19. A. E. P. Veldman, 'Liquid sloshing under low-g conditions: mathematical model and basic numerical method', *NLR Report TR 79057 U*, 1979.
20. J. E. Welch, F. H. Harlow, J. P. Shannon and B. J. Daly, 'The MAC method: a computing technique for solving viscous, incompressible, transient fluid-flow problems involving free surfaces', *Los Alamos Scientific Laboratory Report LA-3425*, 1966.
21. F. H. Harlow and J. F. Welch, 'Numerical calculation of time-dependent viscous incompressible flow of fluid with free surface', *Phys. Fluids*, **8**, 2182 (1965).
22. H. Miyata and S. Nishimura, 'Finite-difference simulation of nonlinear ship waves', *J. Fluid Mech.*, **157**, 327 (1985).
23. H. Miyata, 'Finite-difference simulation of breaking waves', *J. Comput. Phys.*, **65**, 179 (1986).
24. C. W. Hirt and B. D. Nichols, 'Volume of fluid (VOF) method for the dynamics of free boundaries', *J. Comput. Phys.*, **39**, 201 (1981).
25. B. D. Nichols, C. W. Hirt and R. S. Hotchkiss, 'SOLA-VOF: a solution algorithm for transient fluid flow with multiple free boundaries', *Los Alamos Scientific Laboratory Report LA8355*, 1980.
26. M. D. Torrey, L. D. Cloutman, R. C. Mjolsness and C. W. Hirt, 'NASA-VOF2D: a computer program for incompressible flows with free surfaces', *Los Alamos National Laboratory Report LA-10612-MS*, 1985.
27. W. F. Noh, in B. Adler, S. Fernbach and M. Rotenberg (eds), *Methods in Computational Physics*, Vol. 3, 1964, p. 117.
28. W. F. Noh and P. Woodward, 'SLIC (simple line interface calculation)', in A. I. van de Vooren and P. J. Zandbergen (eds), *Lecture Notes in Physics*, Vol. 59, *Proc. Fifth Int. Conf. on Numerical Methods in Fluid Dynamics*, Springer, New York, 1976, pp. 330–340.
29. A. J. Chorin, 'Flame advection and propagation algorithm', *J. Comput. Phys.*, **35**, 1 (1980).
30. A. J. Chorin, 'Curvature and solidification', *J. Comput. Phys.*, **57**, 472 (1985).
31. N. Ashgriz and J. Y. Poo, 'FLAIR: flux line-segment model for advection and interface reconstruction', *J. Comput. Phys.*, **93**, 449 (1991).
32. F. Mashayek and N. Ashgriz, 'Advection of axisymmetric interfaces by the volume-of-fluid method', *Int. j. numer. methods fluids*, **20**, 1337–1361 (1995).
33. T. J. R. Hughes, W. K. Liu and A. Brooks, 'Finite element analysis of incompressible viscous flows by the penalty function formulation', *J. Comput. Phys.*, **30**, 1–60 (1979).
34. W. R. Buell and B. A. Bush, 'Mesh generations—a survey', *ASME J. Ind. Eng. B*, **95**, 332 (1973).
35. R. Haber, M. S. Shephard, J. F. Abel, R. H. Gallagher and D. P. Greenberg, 'A general two-dimensional, graphical finite element preprocessor utilizing discrete transfinite mapping', *Int. j. numer. methods eng.*, **17**, 1015 (1981).
36. T. I.-P. Shih, R. T. Bailey, H. L. Nguyen and R. J. Roelke, 'Algebraic grid generation for complex geometries', *Int. j. numer. methods eng.*, **13**, 1 (1991).
37. C. Chinnaswamy, B. Amadei and T. H. Illangasekare, 'A new method for finite element transitional mesh generation', *Int. j. numer. methods eng.*, **31**, 1253 (1991).
38. L. A. Crivelli and S. R. Idelsohn, 'A temperature-based finite element solution for phase-change problems', *Int. j. numer. methods eng.*, **23**, 99 (1986).
39. S. O. Unverdi and G. Tryggvason, 'A front-tracking method for viscous, incompressible, multi-fluid flows', *J. Comput. Phys.*, **100**, 25 (1992).
40. J. U. Brackbill, D. B. Kothe and C. Zemach, 'A continuum method for modeling surface tension', *J. Comput. Phys.*, **100**, 335 (1992).
41. W. S. Rayleigh, 'On the instability of jets', *Proc. Lond. Math. Soc.*, **10**, 4–13 (1879).

42. M. C. Yuen, 'Non-linear capillary instability of a liquid jet', *J. Fluid Mech.*, **33**, 151–163 (1968).
43. S. Chandrasekhar, *Hydrodynamic and Hydromagnetic Stability*, Clarendon, Oxford, 1961.
44. E. F. Goedde and M. C. Yuen, 'Experiments on liquid jet instability', *J. Fluid Mech.*, **40**, 495–511 (1970).
45. P. Vassallo and N. Ashgriz, 'Satellite formation and merging in liquid jet breakup', *Proc. R. Soc. Lond. A*, **433**, 269–286 (1991).
46. N. N. Mansour and T. S. Lundgren, 'Satellite formation in capillary jet breakup', *Phys. Fluids A*, 2 1141–1144 (1990).
47. N. Ashgriz and J. Y. Poo, 'Coalescence and separation in binary collisions of liquid drops', *J. Fluid Mech.*, **221**, 183 (1990).
48. J. Y. Poo and N. Ashgriz, 'Numerical simulation of collision of two-dimensional drops', *Proc. 5th Ann. Conf. on Liquid Atomization and Spray Systems*, 1992.